Improved Limits on Scattering of Weakly Interacting Massive Particles from Reanalysis of 2013 LUX Data

D. S. Akerib,[1,2,3] H. M. Araújo,[4] X. Bai,[5] A. J. Bailey,[4] J. Balajthy,[6] P. Beltrame,[7] E. P. Bernard,[8] A. Bernstein,[9] T. P. Biesiadzinski,[1,2,3] E. M. Boulton,[8] A. Bradley,[1] R. Bramante,[1,2,3] S. B. Cahn,[8] M. C. Carmona-Benitez,[10] C. Chan,[11] J. J. Chapman,[11] A. A. Chiller,[12] C. Chiller,[12] A. Currie,[4,*] J. E. Cutter,[13] T. J. R. Davison,[7] L. de Viveiros,[14] A. Dobi,[15] J. E. Y. Dobson,[16] E. Druszkiewicz,[17] B. N. Edwards,[8] C. H. Faham,[15] S. Fiorucci,[15] R. J. Gaitskell,[11] V. M. Gehman,[15] C. Ghag,[16] K. R. Gibson,[1] M. G. D. Gilchriese,[15] C. R. Hall,[6] M. Hanhardt,[5,18] S. J. Haselschwardt,[10] S. A. Hertel,[19,8,15] D. P. Hogan,[19] M. Horn,[19,8,15] D. Q. Huang,[11] C. M. Ignarra,[2,3] M. Ihm,[19,15] R. G. Jacobsen,[19,15] W. Ji,[1,2,3] K. Kazkaz,[9] D. Khaitan,[17] R. Knoche,[6] N. A. Larsen,[8] C. Lee,[1,2,3] B. G. Lenardo,[13,9] K. T. Lesko,[15] A. Lindote,[14] M. I. Lopes,[14] D. C. Malling,[11] A. Manalaysay,[13] R. L. Mannino,[20] M. F. Marzioni,[7] D. N. McKinsey,[19,8,15] D.-M. Mei,[12] J. Mock,[21] M. Moongweluwan,[17] J. A. Morad,[13] A. St. J. Murphy,[7] C. Nehrkorn,[10] H. N. Nelson,[10] F. Neves,[14] K. O'Sullivan,[15,19,8] K. C. Oliver-Mallory,[19,15] R. A. Ott,[13] K. J. Palladino,[22,2,3] M. Pangilinan,[11] E. K. Pease,[19,8,15] P. Phelps,[1] L. Reichhart,[16] C. Rhyne,[11] S. Shaw,[16] T. A. Shutt,[1,2,3] C. Silva,[14] V. N. Solovov,[14] P. Sorensen,[15] S. Stephenson,[13] T. J. Sumner,[4] M. Szydagis,[21] D. J. Taylor,[18] W. Taylor,[11] B. P. Tennyson,[8] P. A. Terman,[20] D. R. Tiedt,[5] W. H. To,[1,2,3] M. Tripathi,[13] L. Tvrznikova,[19,8,15] S. Uvarov,[13] J. R. Verbus,[11] R. C. Webb,[20] J. T. White,[20] T. J. Whitis,[1,2,3] M. S. Witherell,[10] F. L. H. Wolfs,[17] K. Yazdani,[4] S. K. Young,[21] and C. Zhang[12]

(LUX Collaboration)

[1]*Case Western Reserve University, Department of Physics, 10900 Euclid Ave, Cleveland, Ohio 44106, USA*
[2]*SLAC National Accelerator Laboratory, 2575 Sand Hill Road, Menlo Park, California 94205, USA*
[3]*Kavli Institute for Particle Astrophysics and Cosmology, Stanford University, 452 Lomita Mall, Stanford, California 94309, USA*
[4]*Imperial College London, High Energy Physics, Blackett Laboratory, London SW7 2BZ, United Kingdom*
[5]*South Dakota School of Mines and Technology, 501 East St Joseph St., Rapid City, South Dakota 57701, USA*
[6]*University of Maryland, Department of Physics, College Park, Maryland 20742, USA*
[7]*SUPA, School of Physics and Astronomy, University of Edinburgh, Edinburgh EH9 3FD, United Kingdom*
[8]*Yale University, Department of Physics, 217 Prospect St., New Haven, Connecticut 06511, USA*
[9]*Lawrence Livermore National Laboratory, 7000 East Ave., Livermore, California 94551, USA*
[10]*University of California Santa Barbara, Department of Physics, Santa Barbara, California 93106, USA*
[11]*Brown University, Department of Physics, 182 Hope St., Providence, Rhode Island 02912, USA*
[12]*University of South Dakota, Department of Physics, 414E Clark St., Vermillion, South Dakota 57069, USA*
[13]*University of California Davis, Department of Physics, One Shields Ave., Davis, California 95616, USA*
[14]*LIP-Coimbra, Department of Physics, University of Coimbra, Rua Larga, 3004-516 Coimbra, Portugal*
[15]*Lawrence Berkeley National Laboratory, 1 Cyclotron Rd., Berkeley, California 94720, USA*
[16]*Department of Physics and Astronomy, University College London, Gower Street, London WC1E 6BT, United Kingdom*
[17]*University of Rochester, Department of Physics and Astronomy, Rochester, New York 14627, USA*
[18]*South Dakota Science and Technology Authority, Sanford Underground Research Facility, Lead, South Dakota 57754, USA*
[19]*University of California Berkeley, Department of Physics, Berkeley, California 94720, USA*
[20]*Texas A&M University, Department of Physics, College Station, Texas 77843, USA*
[21]*University at Albany, State University of New York, Department of Physics, 1400 Washington Avenue, Albany, New York 12222, USA*
[22]*University of Wisconsin-Madison, Department of Physics, 1150 University Avenue, Madison, Wisconsin 53706, USA*
(Received 12 December 2015; revised manuscript received 8 March 2016; published 20 April 2016)

We present constraints on weakly interacting massive particles (WIMP)-nucleus scattering from the 2013 data of the Large Underground Xenon dark matter experiment, including 1.4×10^4 kg day of search exposure. This new analysis incorporates several advances: single-photon calibration at the scintillation wavelength, improved event-reconstruction algorithms, a revised background model including events originating on the detector walls in an enlarged fiducial volume, and new calibrations from decays of an injected tritium β source and from kinematically constrained nuclear recoils down to 1.1 keV. Sensitivity, especially to low-mass WIMPs, is enhanced compared to our previous results which modeled the

signal only above a 3 keV minimum energy. Under standard dark matter halo assumptions and in the mass range above 4 GeV c^{-2}, these new results give the most stringent direct limits on the spin-independent WIMP-nucleon cross section. The 90% C.L. upper limit has a minimum of 0.6 zb at 33 GeV c^{-2} WIMP mass.

DOI: 10.1103/PhysRevLett.116.161301

Consistent evidence from a range of astrophysical observations suggests that cold dark matter is the dominant form of matter in our Galaxy and in the Universe overall [1–3]. Weakly interacting massive particles (WIMPs) are a generic class of dark matter candidate and may be detectable via weak-force-mediated nuclear recoils in detectors on Earth [4,5]. In October 2013, the LUX collaboration reported results from a 85.3 live-day exposure of a 118 kg fiducial mass [6]. These remain the strongest constraints on the spin-independent WIMP-nucleon cross section over a wide range of WIMP mass. They were, however, determined under the pessimistic assumption of zero efficiency for nuclear recoil (NR) events below 3 keV, which was the minimum energy at which liquid xenon had been calibrated at that time. Here, we present a new analysis of the data reported in [6] which accounts for the recent *in situ* calibration of NR energies well below 3 keV. Event reconstruction and models of background are improved, and a further 10 days of exposure are also added. Together, these updates greatly enhance sensitivity to low-mass WIMPs, exploring a new region of dark matter parameter space.

LUX (Large Underground Xenon) is a dual-phase xenon time-projection chamber (TPC) with 250 kg of active liquid mass, designed to observe WIMPs in the local halo scattering on xenon nuclei. Energy thus deposited creates a primary scintillation signal, called $\mathcal{S}1$, and ionization charge which drifts vertically in an electric field to produce an electroluminescence signal in the gas phase, called $\mathcal{S}2$. Both signals are detected by photomultiplier tubes (PMTs), 61 viewing the TPC from above and 61 from below. A description of the detector and its deployment at the Sanford Underground Research Facility can be found in [7].

This update includes several refinements to the initial data processing, whereby PMT waveforms are calibrated in units of detected photons (phd). The pulse area estimation was further improved to reduce the impact of two small systematic effects. A coherent noise artifact consistently appeared in some channels and is now subtracted. This correction to each $\mathcal{S}1$ or $\mathcal{S}2$ pulse ranged from 0 to 0.2 phd per channel. The baseline estimates of the data-acquisition firmware were also found to introduce a small arithmetic-truncation error which was corrected. The mean waveform area of one detected photon within each PMT is calibrated using a sample of $\mathcal{S}1$s below 10 phd total and near the detector center, after a <5% correction for photon pileup. A separate single-photon measurement is made using the electroluminescence light of single electrons (SEs). The mean over all PMTs agrees within 2.5% between the two measurements. Compared to a previous calibration using pulsed 440 nm LEDs, these xenon light methods avoid pulser cross talk, avoid systematic error from assumed distributions by using sample means rather than parametric fits, and automatically account for wavelength-dependent double-photoelectron emission by single photons at the photocathode [8].

Candidate single-scatter active-region events are termed "golden", and consist of one $\mathcal{S}2$ preceded by one $\mathcal{S}1$.

$\mathcal{S}1$ light in the WIMP region of interest is quantified using both calibrated pulse areas and pulse counting, whereby candidate single photons ("spikes") are identified in sparse waveforms. In addition to photon statistics, pulse areas include fluctuations due to gain variance and single- versus double-photoelectron emission at the photocathode. Therefore, counting discrete waveform spikes can give a more precise scintillation measurement over using integrated pulse areas. A parametrization of the maximum-likelihood number of photons, as a function of area and spike count, is computed from simulated pileup in time and measured photon area distributions. For $\mathcal{S}1$s above 20 keV electron-recoil (ER) equivalent energy and for all $\mathcal{S}2$s, where pileup is prevalent, detected photons are estimated using pulse area alone. The drift time between $\mathcal{S}1$ and $\mathcal{S}2$ gives the vertical location of each event to millimeter precision ($\sigma = 0.9$ mm measured with coincident Bi-Po decays [9]). $\mathcal{S}2$ positions in the x-y plane are estimated using data-derived parametrizations of individual top-array PMT responses [10]. The gate and cathode electrode grids establish a field, with a mean and range in the fiducial volume of 180 ± 20 V cm^{-1}, to drift charge from the active volume towards the liquid surface. The field is nonuniform due to geometric effects similar to [11]. A weak radial component moves drifting electrons inwards from the site of ionization by up to 4.6 cm for the outer bottom edge of the fiducial volume, in agreement with an electrostatic model of the drift field [12]. We account for this effect by exploiting the spatial uniformity of a ^{83m}Kr calibration source [13,14] to derive a mapping between $\mathcal{S}2$ and vertex position. Position variables used in later analysis refer to the reconstructed vertex: the standard deviations of the reconstructed x and y have a statistical contribution of 10 mm at the $\mathcal{S}2$ threshold, and a 5 mm systematic contribution

estimated from the reconstruction of the chamber walls and of a collimated neutron beam [15].

Weekly calibrations with the monoenergetic ^{83m}Kr source are used to derive, from the estimates of detected photons and event position, two corrected variables, called $S1$ and $S2$, which equalize detector response throughout the active volume. They are proportional, respectively, to the scintillation light and ionization charge leaving the interaction site. By convention, $S1$ equals the raw number of detected photons for events at the center of the detector. Similarly, events at the center would, in the absence of signal charge loss to impurities during drifting, have a mean of $S2$ detected $\mathcal{S}2$ photons. Calibration relative to these reference points accounts for position dependence in the efficiency to extract an electron into the gas, electroluminescence yield, and photon-detection efficiency, and for time-dependent xenon purity. In [6], ionization was estimated using only the bottom PMT array, over which $\mathcal{S}2$ light is quite uniform. However, a subsequent large-sample calibration with a dissolved tritiated methane source [16] has demonstrated that using all PMTs reduces by 20% the rate of leakage ER events below the Gaussian mean $\log(S2/S1)$ of NR calibration at a given $S1$. We find that, after flat fielding, the reduced variance from measuring more photons outweighs residual nonuniformity in the top array response. The sum of top and bottom arrays is thus adopted for $S2$.

The detector-specific gain factors g_1 and g_2 are defined via the expectation values $\langle S1\rangle = g_1 n_\gamma$ and $\langle S2\rangle = g_2 n_e$, given n_γ initial photons and n_e initial electrons leaving the interaction site. Their values in LUX were obtained by the technique of [17] using a set of monoenergetic electron-recoil sources as in [18]. The sum of the photon yield and the electron yield is observed to be constant with energy, equal to the reciprocal of the W value as defined in [19]; however, the individual yields do vary, because charge recombination probability depends upon energy, E. In a plot of $S2/E$ versus $S1/E$, the sources trace a line and a fit to this line measures the gain factors: $g_1 = (0.117 \pm 0.003)$ phd per photon and $g_2 = (12.1 \pm 0.8)$ phd per electron, with anticorrelation $\rho = -0.6$. Calibrating $S1$ and g_1 in units of detected VUV photons results in a numerical shift relative to the previous, smaller units of photoelectrons (phe) but is preferred because g_1 thus defined is the probability for an initial photon to cause a detectable PMT response. Using yields at many discrete energies is also more robust than the single spectral fit used to estimate values of $g_1 = (0.14 \pm 0.01)$ phe per photon and $g_2 = (16.0 \pm 0.3)$ phe per electron in [6].

The fiducial range in drift time, mitigating radiogenic backgrounds from detector materials, is unchanged from [6] at 38–305 μs (48.6–8.5 cm above the faces of the bottom PMTs in z). A data-driven model of events originating on detector sidewalls allows a larger fiducial radius of 20 cm. The fiducial mass was measured as a fraction of the known active xenon mass by counting tritium events: the result of (145.4 ± 1.3) kg is consistent with the 147 kg expected from geometry. $\mathcal{S}1$ pulses are required to have two-PMT coincidence and $S1$ in the range 1–50 phd. Normalizing to the detector center means that $S1$ can be below 2.0 phd even with two photons detected. A lower analysis threshold of 165 phd raw $\mathcal{S}2$ size (6.7 times the mean SE response) is applied to mitigate the random coincidence background from smaller, isolated $\mathcal{S}2$s.

The LUX NR response in $S2$ and $S1$ has been measured *in situ* using monoenergetic neutrons from an Adelphi DD108 deuterium-deuterium (D-D) fusion source.

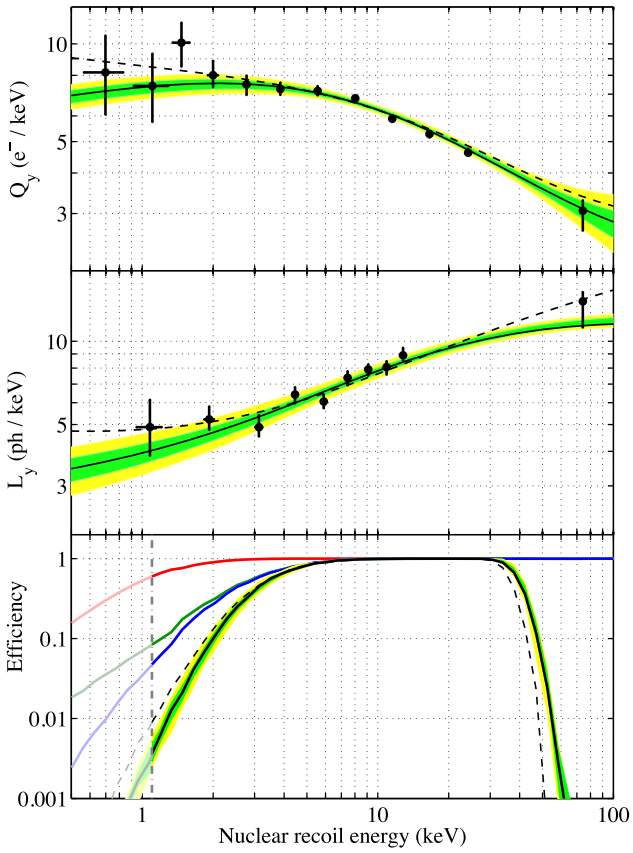

FIG. 1. *Top, middle* Yields of electrons and photons, respectively, for nuclear recoils in LUX, measured *in situ* with D-D neutrons. Error bars are statistical. *Bottom:* efficiencies for NR event detection, averaged over the fiducial volume and estimated using LUXSim with parameters tuned to D-D calibration. In descending order of efficiency—red: detection of an $\mathcal{S}2$ ($\geq$2 electrons emitted); green: detection of an $\mathcal{S}1$ ($\geq$2 PMTs detecting photons); blue: detection of both an $\mathcal{S}1$ and an $\mathcal{S}2$; black: detection passing thresholds in $S1$ and raw $\mathcal{S}2$ size. The $97.5\% \pm 1.7\%$ event-classification efficiency is applied as an additional, energy-independent scaling. The vertical line at 1.1 keV marks the low-energy cutoff applied in the signal model. *All panels:* solid lines show the best fit of the Lindhard parametrization; shaded regions span its 1- and 2-σ uncertainty used for the final result. Dashed lines show the best fit of the alternate, Bezrukov NR parametrization.

The yields are presented in Fig. 1. The dominant systematics in these charge and light calibrations correspond to a uniform 9% and 3%, respectively [15,20,21]. The NR response in $S2$ was measured with an absolute determination of the deposited energy from scattering angles in multiple-vertex events. This calibration of the NR signal yields directly improves sensitivity to low-mass WIMPs over [6].

To compute WIMP signal probability density functions (PDFs) from the D-D calibration and account for uncertainty, an empirical response model was fitted simultaneously to the yields and to the median $S2$ versus $S1$ of single-scatter NR events. The mean fraction of recoil energy lost to electrons, $\mathcal{L}(E)$, is described by the Lindhard model [22]. Scintillation and ionization quanta leaving the track are described by an energy-independent ratio of initial excitons and ions, followed by charge recombination according to the Thomas-Imel box model [23] and biexcitonic quenching including Penning ionization [24,25]. $S1$ and $S2$ are then generated via standard statistical distributions which model stages of detector response (collection of scintillation photons, attenuation of the ionization signal before $\mathcal{S}2$ production, photoelectron and SE distributions). The full model is described in [15] and the fit procedure follows [26]. An alternate parametrization of $\mathcal{L}(E)$ by Bezrukov *et al.* [27] is similarly consistent with calibration data and implies higher signal efficiency at low energies; it is shown for reference but does not enter into the reported limit. Figure 1 shows the best fits to experimental yields of signal quanta for both parametrizations.

Nuclear-recoil energy spectra for the WIMP signal are derived from a standard Maxwellian velocity distribution with $v_0 = 220\,\mathrm{km/s}$, $v_{\mathrm{esc}} = 544$ km/s, $\rho_0 = 0.3$ GeV/cm^3, average Earth velocity during data taking of 245 km/s, and a Helm form factor, as in [6]. Following the same criterion as that analysis, but with new calibration data, the signal spectrum is assumed zero below the lowest D-D $S1$ calibration point of 1.1 keV. Signal PDFs and rates as a function of the spin-independent WIMP-nucleon cross section, σ_n, are computed from the empirical NR response model. Uncertainties in the absolute values of g_1 and g_2 do not propagate to the signal model, because it is calibrated *in situ* in the $S1$ and $S2$ variables. The non-negligible signal-model uncertainties are incorporated in the likelihood via two nuisance parameters with Gaussian constraints from the D-D calibration (see Table I): the Lindhard k parameter and the $\mathcal{S}2$ gain during D-D calibration in November 2013 relative to the WIMP search, $g_{2,\mathrm{DD}}/g_{2\mathrm{WS},}$.

The efficiency for WIMP-nuclear recoils to appear as events in the search data is the product of several detection stages. Modeling the WIMP signal only above 1.1 keV includes 0.3% of the recoil spectrum for a 4 GeV c^{-2} WIMP, rising to 94% in the high-mass limit. The efficiency to generate an $\mathcal{S}1$ and an $\mathcal{S}2$ passing all analysis thresholds in the best-fit NR model, shown along with systematic variations in Fig. 1, rises from 0.3% at the 1.1 keV cutoff to 50% at 3.3 keV. Finally, identification of $\mathcal{S}1$ and $\mathcal{S}2$ within real waveforms can fail in ways not reproduced by simulation, for instance, where the hit-pattern or pulse-shape variables used in classification are biased by PMT afterpulsing. The probability to thus discard events was found by visually inspecting 4000 AmBe calibration events: the pulse-identification efficiency for events in the WIMP region of interest and passing the analysis thresholds was found to be $97.5\% \pm 1.7\%$, and is implemented as an energy-independent scaling.

TABLE I. Nuisance parameters in the global best fit to 95-day search data. Constraints are Gaussian with means and standard deviations indicated. Event counts are after cuts and analysis thresholds. The best-fit model has zero contribution from the signal PDF. In this case, the signal-model parameters simply float to the central values of their constraints, and so are not listed.

Parameter	Constraint	Fit value
Lindhard k	0.174 ± 0.006	⋯
$\mathcal{S}2$ gain ratio: $g_{2,\mathrm{DD}}/g_{2\mathrm{WS},}$	0.94 ± 0.04	⋯
Low-z-origin γ counts: $\mu_{\gamma,\mathrm{bottom}}$	172 ± 74	165 ± 16
Other γ counts: $\mu_{\gamma,\mathrm{rest}}$	247 ± 106	228 ± 19
β counts: μ_β	55 ± 22	84 ± 15
^{127}Xe counts: $\mu_{\mathrm{Xe\text{-}127}}$	91 ± 27	78 ± 12
^{37}Ar counts: $\mu_{\mathrm{Ar\text{-}37}}$	⋯	12 ± 8
Wall counts: μ_{wall}	24 ± 7	22 ± 4

Radiogenic backgrounds are again estimated as in [28], but with the revised data-reduction techniques and cuts. The added acceptance increases the expected neutron background to 0.08 ± 0.01 NR events in the WIMP-search sample. Random coincidence of isolated $\mathcal{S}1$s (having rate 1 s^{-1}) and $\mathcal{S}2$s (5×10^{-4} s^{-1}) within a physical drift time causes an expected 1.1 events in the full search range of $S1$ and $S2$. Coherent neutrino-nucleus scattering by ^{8}B solar neutrinos contributes 0.10 (0.16) golden events under the Lindhard (Bezrukov) yield model. None of these small background populations are included in the model.

Isolated low-energy ER events in the fiducial volume arise from four sources: Compton scattering of γ rays from detector component radioactivity, ^{85}Kr or Rn-daughter contaminants in the liquid undergoing β decay with no accompanying γ rays detected, x rays following those ^{127}Xe electron-capture decays where the coincident γ ray escapes the xenon, and a line at 2.8 keV, evident due to the improved energy resolution and consistent with electron-capture decays in the fiducial volume by ^{37}Ar nuclei. Measurements of the ^{37}Ar concentration in lab air are planned and will, together with limits on air leaks from xenon sampling results, give an upper limit on rate; it is currently an unconstrained fit parameter.

The Geant4-based LUXSim package, incorporating the NEST model for signal generation in the xenon [29–32],

was tuned to the $S1$-$S2$ distribution of 1.8×10^5 fiducial-volume electron recoils from the internal tritium source. Good agreement was obtained from threshold to the 18.6 keV end point, well above the WIMP signal in both light and charge, and the reconstructed β spectrum validates the g_1 and g_2 values measured with line sources [16]. Simulated waveforms, processed with the same data-reduction software and event selection as applied to the search data, are used to model the ER backgrounds in $S1$ and $S2$.

Events due to detector component radioactivity, both within and above the energy region of interest, were simulated with LUXSim. The high-energy spectral agreement between data and simulation based on γ screening is generally good [20,28]; however, we observe an excess of ER events with 500–1500 keV energy concentrated in the lowest 10 cm of the active region. Its precise origin is unknown but the spectrum can be reproduced by simulating additional, heavily downscattered ^{238}U chain, ^{232}Th chain, and ^{60}Co γ rays in the center of a large copper block below the PMTs. This implies an extra 105 low-energy Compton-scatter events, included in the background model. The γ-ray population is subdivided into two spatial distributions with floating normalization: one generated by the bottom PMT array, its support structure, and the bottom γ-ray shield; and one from the rest of the detector.

A final source of background, newly modeled here, is the tail in reconstructed r of events on the PTFE sidewalls. The $S1$-$S2$ distribution of background events on the walls differs from that in the liquid bulk. Charge collection is incomplete, so the ER population extends to lower values of $S2$. There are, in addition, true nuclear recoils from the daughter ^{206}Pb nuclei of α decay by ^{210}Po plated on the wall. The leakage of wall events towards smaller r depends strongly, via position resolution, on $\mathcal{S}2$ size. The wall population in the fiducial volume thus appears close to the $\mathcal{S}2$ threshold, largely below the signal population in $S2$ at given $S1$. It is modeled empirically using high-r and low-$S2$ sidebands in the search data [33].

Systematic uncertainties in background rates are treated via nuisance parameters in the likelihood: their constraints are listed with other fit parameters in Table I. $S1$, $S2$, z, and r are each useful discriminants against backgrounds, and cross sections are tested via the likelihood of the search events in these four observables.

Search data were acquired between April 24th and September 1st, 2013. Two classes of cuts based on prevailing detector conditions assure well-measured events in both low-energy calibration and WIMP-search samples. Firstly, data taken during excursions in macroscopic detector properties, such as xenon circulation outages or instability of applied high voltage, are removed, constituting 0.8% of gross live time. Secondly, an upper threshold is imposed on summed pulse area during the event window but outside $\mathcal{S}1$ and $\mathcal{S}2$. It removes triggers during the aftermath of photoionization and delayed electron emission following large $\mathcal{S}2$s. The threshold is set for >99% tritium acceptance and removes 1% of gross live time [34]. We report on 95.0 live days. Figure 2 shows the measured light and charge of the 591 surviving events in the fiducial volume.

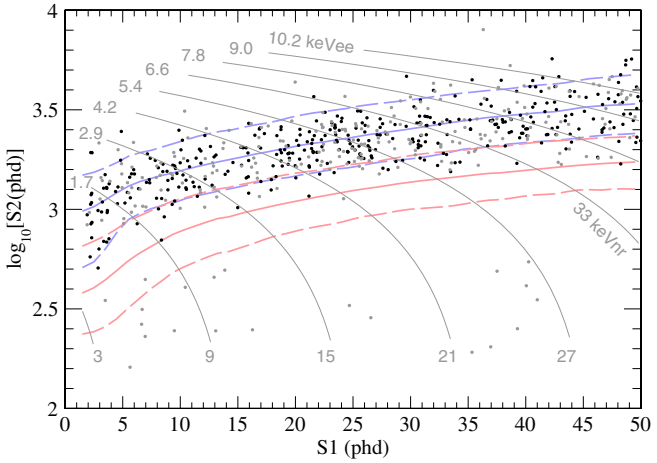

FIG. 2. Observed events in the 2013 LUX exposure of 95 live days and 145 kg fiducial mass. Points at <18 cm radius are black; those at 18–20 cm are gray. Distributions of uniform-in-energy electron recoils (blue) and an example 50 GeV c^{-2} WIMP signal (red) are indicated by 50th (solid), 10th, and 90th (dashed) percentiles of $S2$ at given $S1$. Gray lines, with ER scale of keVee at top and Lindhard-model NR scale of keVnr at bottom, are contours of the linear combined $S1$-and-$S2$ energy estimator [19].

A double-sided, profile-likelihood-ratio (PLR) statistic [35] is employed to test signal hypotheses. For each WIMP mass, we scan over cross section to construct a 90% confidence interval, with test statistic distributions evaluated by Monte Carlo sampling using the RooStats package [36]. At all masses, the maximum-likelihood value of σ_n is found to be zero. The background-only model gives a good fit to the data, with KS test p values of 0.05, 0.07, 0.34, and 0.64 for the projected distributions in $S1$, $S2$, r, and z respectively. Upper limits on cross section for WIMP masses from 4 to 1000 GeV c^{-2} are shown in Fig. 3; above, the limit increases in proportion to mass until $\gtrsim 10^8$GeV c^{-2}, 10^6 zb, where the Earth begins to attenuate the WIMP flux. The raw PLR result lies between one and two Gaussian σ below the expected limit from background trials. We apply a power constraint [37] at the median so as not to exclude cross sections for which sensitivity is low through chance background fluctuation. We include systematic uncertainties in the nuclear recoil response in the PLR, which has a modest effect on the limit with respect to assuming the best-fit model exactly: less than 20% at all masses. Limits calculated with the alternate, Bezrukov parametrization would be 0.48, 1.02, and 1.05 times the reported ones at 4, 33, and 1000 GeV c^{-2}, respectively. Uncertainties in the assumed dark matter halo are beyond the scope of this

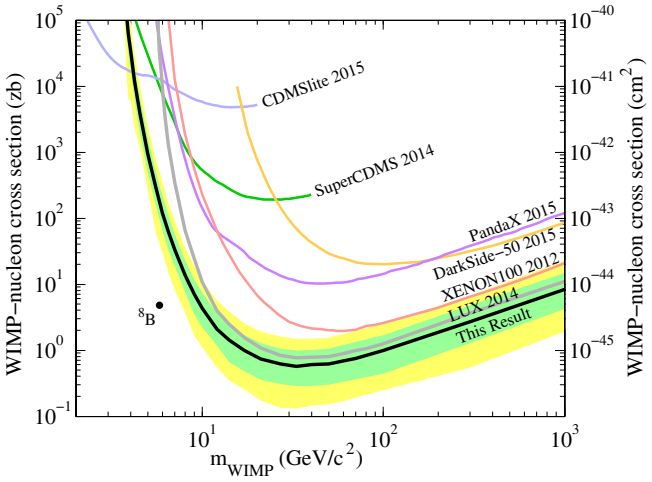

FIG. 3. Upper limits on the spin-independent elastic WIMP-nucleon cross section at 90% C.L. Observed limit in black, with the 1- and 2-σ ranges of background-only trials shaded green and yellow. Also shown are limits from the first LUX analysis [6] (gray), SuperCDMS [40] (green), CDMSlite [41] (light blue), XENON100 [42] (red), DarkSide-50 [43] (orange), and PandaX [44] (purple). The expected spectrum of coherent neutrino-nucleus scattering by ^{8}B solar neutrinos can be fit by a WIMP model as in [45], plotted here as a black dot.

Letter but are reviewed in, e.g., [38]. Limits on spin-dependent cross sections are presented elsewhere [39].

In conclusion, reanalysis of the 2013 LUX data has excluded new WIMP parameter space. The added fiducial mass and live time, and better resolution of light and charge yield a 23% improvement in sensitivity at high WIMP masses over the first LUX result. The reduced, 1.1 keV cutoff in the signal model improves sensitivity by 2% at high masses but is the dominant effect below 20 GeV c^{-2}, and the range 5.2 to 3.3 GeV c^{-2} is newly demonstrated to be detectable in xenon. These techniques further enhance the prospects for discovery in the ongoing 300-day LUX search and the future LUX-ZEPLIN [46] experiment.

This work was partially supported by the U.S. Department of Energy (DOE) under Awards No. DE-FG02-08ER41549, No. DE-FG02-91ER40688, No. DE-FG02-95ER40917, No. DE-FG02-91ER40674, No. DE-NA0000979, No. DE-FG02-11ER41738, No. DE-SC0006605, No. DE-AC02-05CH11231, No. DE-AC52-07NA27344, and No. DE-FG01-91ER40618; the U.S. National Science Foundation under Grant No. PHYS-0750671, No. PHY-0801536, No. PHY-1004661, No. PHY-1102470, No. PHY-1003660, No. PHY-1312561, No. PHY-1347449; the Research Corporation Grant No. RA0350; the Center for Ultra-low Background Experiments in the Dakotas (CUBED); and the South Dakota School of Mines and Technology (SDSMT). LIP-Coimbra acknowledges funding from Fundação para a Ciência e a Tecnologia (FCT) through the Project-Grant No. PTDC/FIS-NUC/1525/2014. Imperial College and Brown University thank the UK Royal Society for travel funds under the International Exchange Scheme (IE120804). The UK groups acknowledge institutional support from Imperial College London, University College London and Edinburgh University, and from the Science and Technology Facilities Council for PhD Studentships No. ST/K502042/1 (AB), No. ST/K502406/1 (SS), and No. ST/M503538/1 (KY). The University of Edinburgh is a charitable body, registered in Scotland, with Registration No. SC005336. This research was conducted using computational resources and services at the Center for Computation and Visualization, Brown University. We gratefully acknowledge the logistical and technical support and the access to laboratory infrastructure provided to us by the Sanford Underground Research Facility (SURF) and its personnel at Lead, South Dakota. SURF was developed by the South Dakota Science and Technology Authority, with an important philanthropic donation from T. Denny Sanford, and is operated by Lawrence Berkeley National Laboratory for the Department of Energy, Office of High Energy Physics. We thank Felix Kahlhoefer and Sebastien Wild for uncovering a mistake in a preprint of this work.

*Corresponding author.
alastair.currie08@imperial.ac.uk

[1] J. I. Read, The local dark matter density, J. Phys. G **41**, 063101 (2014).
[2] D. Harvey, R. Massey, T. Kitching, A. Taylor, and E. Tittley, The nongravitational interactions of dark matter in colliding galaxy clusters, Science **347**, 1462 (2015).
[3] Ade *et al.* (Planck Collaboration), Planck 2015 results. XIII. Cosmological parameters, arXiv:1502.01589v2.
[4] M. W. Goodman and E. Witten, Detectability of certain dark-matter candidates, Phys. Rev. D **31**, 3059 (1985).
[5] J. L. Feng, Dark matter candidates from particle physics and methods of detection, Annu. Rev. Astron. Astrophys. **48**, 495 (2010).
[6] D. S. Akerib *et al.* (LUX Collaboration), First Results from the LUX Dark Matter Experiment at the Sanford Underground Research Facility, Phys. Rev. Lett. **112**, 091303 (2014).
[7] D. S. Akerib *et al.* (LUX Collaboration), The large underground xenon (LUX) experiment, Nucl. Instrum. Methods Phys. Res., Sect. A **704**, 111 (2013).
[8] C. H. Faham, V. M. Gehman, A. Currie, A. Dobi, P. Sorensen, and R. J. Gaitskell, Measurements of wavelength-dependent double photoelectron emission from single photons in VUV-sensitive photomultiplier tubes, J. Instrum. **10**, P09010 (2015).
[9] C. H. Faham, Ph.D. thesis, Brown University, 2014.
[10] V. Solovov *et al.* (ZEPLIN-III Collaboration), Position reconstruction in a dual phase xenon scintillation detector, IEEE Trans. Nucl. Sci. **59**, 3286 (2012).
[11] Y. Mei, Ph.D. thesis, Rice University, 2011.
[12] D. S. Akerib *et al.* (LUX Collaboration), Calibration, event reconstruction, data analysis and limits calculation for the LUX dark matter experiment (to be published).

[13] L. W. Kastens, S. B. Cahn, A. Manzur, and D. N. McKinsey, Calibration of a liquid xenon detector with $^{83}Kr^{m}$, Phys. Rev. C **80**, 045809 (2009).
[14] A. Manalaysay, T. Marrodán Undagoitia, A. Askin, L. Baudis, A. Behrens, A. D. Ferella, A. Kish, O. Lebeda, R. Santorelli, D. Vénos, and A. Vollhardt, Spatially uniform calibration of a liquid xenon detector at low energies using ^{83m}Kr, Rev. Sci. Instrum. **81**, 073303 (2010).
[15] D. S. Akerib *et al.* (LUX Collaboration), Low energy (0.7–74 keV) nuclear recoil calibration of the LUX dark matter experiment using D-D neutron scattering kinematics (to be published).
[16] D. S. Akerib *et al.* (LUX Collaboration), Tritium calibration of the LUX dark matter experiment, arXiv:1512.03133v1.
[17] T. Doke, A. Hitachi, J. Kikuchi, K. Masuda, H. Okada, and E. Shibamura, Absolute scintillation yields in liquid argon and xenon for various particles, Jpn. J. Appl. Phys. **41**, 1538 (2002).
[18] P. Phelps, Ph.D. thesis, Case Western Reserve University, 2014.
[19] T. Shutt, C. Dahl, J. Kwong, A. Bolozdynya, and P. Brusov, Performance and fundamental processes at low energy in a two-phase liquid xenon dark matter detector, Nucl. Phys. B, Proc. Suppl. **173**, 160 (2007).
[20] D. Malling, Ph.D. thesis, Brown University, 2014.
[21] J. Verbus *et al.*, Proposed low-energy absolute calibration of nuclear recoils in a liquid xenon TPC using D-D neutron scattering kinematics (to be published).
[22] J. Lindhard, V. Nielsen, and M. Scharff, Integral equations governing radiation effects (Notes on Atomic Collisions, III), Mat. Fys. Medd. K. Dan. Vidensk. Selsk **33**, 10 (1963).
[23] J. Thomas and D. A. Imel, Recombination of electron-ion pairs in liquid argon and liquid xenon, Phys. Rev. A **36**, 614 (1987).
[24] A. Hitachi, T. Doke, and A. Mozumder, Luminescence quenching in liquid argon under charged-particle impact: Relative scintillation yield at different linear energy transfers, Phys. Rev. B **46**, 11463 (1992).
[25] D.-M. Mei, Z.-B. Yin, L. Stonehill, and A. Hime, A model of nuclear recoil scintillation efficiency in noble liquids, Astropart. Phys. **30**, 12 (2008).
[26] B. Lenardo, K. Kazkaz, A. Manalaysay, J. Mock, M. Szydagis, and M. Tripathi, A global analysis of light and charge yields in liquid xenon, IEEE Trans. Nucl. Sci. **62**, 3387 (2015).
[27] F. Bezrukov, F. Kahlhoefer, and M. Lindner, Interplay between scintillation and ionization in liquid xenon Dark Matter searches, Astropart. Phys. **35**, 119 (2011).
[28] D. S. Akerib *et al.* (LUX Collaboration), Radiogenic and muon-induced backgrounds in the LUX dark matter detector, Astropart. Phys. **62**, 33 (2015).
[29] S. Agostinelli *et al.*, Geant4—a simulation toolkit, Nucl. Instrum. Methods Phys. Res., Sect. A **506**, 250 (2003).
[30] M. Szydagis, N. Barry, K. Kazkaz, J. Mock, D. Stolp, M. Sweany, M. Tripathi, S. Uvarov, N. Walsh, and M. Woods, NEST: a comprehensive model for scintillation yield in liquid xenon, J. Instrum. **6**, P10002 (2011).
[31] M. Szydagis, A. Fyhrie, D. Thorngren, and M. Tripathi, Enhancement of NEST capabilities for simulating low-energy recoils in liquid xenon, J. Instrum. **8**, C10003 (2013).
[32] D. S. Akerib *et al.* (LUX Collaboration), LUXSim: A component-centric approach to low-background simulations, Nucl. Instrum. Methods Phys. Res., Sect. A **675**, 63 (2012).
[33] C. Lee, Ph.D. thesis, Case Western Reserve University, 2015.
[34] J. Chapman, Ph.D. thesis, Brown University, 2014.
[35] G. Cowan, K. Cranmer, E. Gross, and O. Vitells, Asymptotic formulae for likelihood-based tests of new physics, Eur. Phys. J. C **71**, 1554 (2011).
[36] L. Moneta, K. Belasco, K. S. Cranmer, S. Kreiss, A. Lazzaro, D. Piparo, G. Schott, W. Verkerke, and M. Wolf, The RooStats project, *Proc. Sci.*, ACAT2010 (2010) 057.
[37] G. Cowan, K. Cranmer, E. Gross, and O. Vitells, Power-constrained limits, arXiv:1105.3166.
[38] C. McCabe, Astrophysical uncertainties of dark matter direct detection experiments, Phys. Rev. D **82**, 023530 (2010).
[39] D. S. Akerib *et al.* (LUX Collaboration), Results on the Spin-Dependent Scattering of Weakly Interacting Massive Particles on Nucleons from the Run 3 Data of the LUX Experiment, following Letter, Phys. Rev. Lett. **116**, 161302 (2016).
[40] R. Agnese *et al.* (SuperCDMS Collaboration), Search for Low-Mass Weakly Interacting Massive Particles with SuperCDMS, Phys. Rev. Lett. **112**, 241302 (2014).
[41] R. Agnese *et al.* (SuperCDMS Collaboration), New Results from the Search for Low-Mass Weakly Interacting Massive Particles with the CDMS Low Ionization Threshold Experiment, Phys. Rev. Lett. **116**, 071301 (2016).
[42] E. Aprile *et al.* (XENON100 Collaboration), Dark Matter Results from 225 Live Days of XENON100 Data, Phys. Rev. Lett. **109**, 181301 (2012).
[43] P. Agnes *et al.* (DarkSide Collaboration), Low radioactivity argon dark matter search results from the DarkSide-50 experiment, arXiv:1510.00702
[44] X. Xiao *et al.* (PandaX Collaboration), Low-mass dark matter search results from full exposure of the PandaX-I experiment, Phys. Rev. D **92**, 052004 (2015).
[45] J. Billard, E. Figueroa-Feliciano, and L. Strigari, Implication of neutrino backgrounds on the reach of next generation dark matter direct detection experiments, Phys. Rev. D **89**, 023524 (2014).
[46] D. S. Akerib *et al.* (LZ Collaboration), LUX-ZEPLIN (LZ) conceptual design report, arXiv:1509.02910v2.